

# A study of laser-induced surface defects in silicon and impact on electrical properties

Zeming Sun and Mool C. Gupta<sup>a)</sup>

Charles L. Brown Department of Electrical and Computer Engineering, University of Virginia, Charlottesville, Virginia 22904, USA

(Received 17 September 2018; accepted 20 November 2018; published online 14 December 2018)

Laser processing of silicon solar cells has unique advantages that offer the potential for low-cost high-efficiency photovoltaic devices. The understanding, monitoring, and control of laser-induced defects in silicon become important challenges that limit photovoltaic efficiency. In this work, the fundamental investigation of laser-induced defects was achieved by identifying defect types and origins at different laser-fluence regimes, assessing defect concentrations, and evaluating their impact on surface electrical properties and photovoltaic device performance. Studies showed that below laser melting, little degradation of electrical properties is observed, but no defects are identified; between laser melting and ablation, point defects and oxygen incorporation mainly occur; above laser ablation, dislocations and strain are primarily generated. Laser-induced dislocation density and strain are found likely to increase exponentially with laser fluence, and laser-induced strain is identified to be a possible major source of dislocation generation. In order to understand carrier recombination and charge transport in laser-processed silicon surface, we quantified the drift mobility, conductivity, carrier lifetime, and leakage current at various laser fluences and dislocation levels. The laser-defect induced degradation of surface electrical properties is governed by a probable exponential relationship with laser fluence, suggesting that laser-processing fluences near silicon melting should be carefully chosen for minimizing induced defects and electrical property degradation. Finally, the control of laser-induced defects was demonstrated through laser or furnace post annealing of laser-processed solar cell devices. After two laser-annealing steps, the open circuit voltage, fill factor, series resistance, and shunt resistance were significantly improved, resulting in an increased photovoltaic efficiency. *Published by AIP Publishing.* <https://doi.org/10.1063/1.5058143>

## I. INTRODUCTION

Laser technology plays a significant role in reducing the silicon photovoltaic manufacturing cost.<sup>1</sup> There are several widely-studied laser processes that have been discussed for device fabrication, including laser ablation,<sup>2</sup> laser microtexturing,<sup>3</sup> laser doping,<sup>4</sup> laser-generated passivation,<sup>5</sup> laser-transferred metal contacts,<sup>4,6</sup> laser-fired contacts,<sup>7</sup> and laser annealing.<sup>4,8</sup> These laser processing methods can greatly reduce the fabrication complexity, avoid multiple lithographic patterning steps, and potentially replace high-temperature or high-vacuum processes.

However, laser-induced structural defects become a major challenge in the performance improvement of laser-based photovoltaic<sup>9–11</sup> and microelectronic<sup>12,13</sup> devices. Laser-induced defects can dramatically degrade the electrical properties of laser-processed silicon. In particular, laser-induced defects can limit the minority carrier lifetime,<sup>14,15</sup> increase the leakage current,<sup>11,13,16</sup> and adversely affect the device performance.<sup>10,15</sup> Laser processing is generally limited to the surface region where most of the light absorption occurs. Several experimental studies<sup>16–18</sup> showed that laser-induced defects are concentrated roughly in the laser heated region, and the modeling study<sup>19</sup> confirmed the

heating depth is approximately 10  $\mu\text{m}$  when using a 1060 nm wavelength, 50 ns pulse width laser beam. Thus, it is of fundamental interest to investigate the surface electrical properties in the laser-processed silicon. Yet, such surface analysis of carrier recombination and charge transport remain difficult. The correlation between the laser-induced defect generation and surface electrical properties is one of the motivations of this study.

Moreover, due to the rapid development of high power lasers and improved wafer quality, previous laser-induced damage studies cannot provide sufficient information to guide current laser-based Si photovoltaic and microelectronic applications. In recent work, researchers<sup>20</sup> focus on the ultrafast-laser induced damage. However, the nanosecond-lasers, which dominate laser-based silicon photovoltaic applications, lack comprehensive investigations on induced structural defects. In limited examples, Hameiri *et al.*<sup>9</sup> and Ohmer *et al.*<sup>21</sup> focused on the laser-induced defect formation in the laser doping technique. Hence, for a wider acceptance of broader laser-based applications, a fundamental material-level study of nanosecond-laser-processed Si is necessary to understand the defect generation mechanisms and identify the damage-limiting laser conditions, which is another motivation for this study.

Laser-induced defects include point defects,<sup>22</sup> dislocations,<sup>8,23</sup> microtwins,<sup>24</sup> phase changes,<sup>24</sup> oxygen incorporation,<sup>14,25</sup> and internal strain.<sup>15,24</sup> Recent studies have

<sup>a)</sup>E-mail: [mgupta@virginia.edu](mailto:mgupta@virginia.edu)

emphasized the device performance degradation due to laser-induced defects. Hameiri *et al.*<sup>9</sup> indicated that the choice of dielectric films for laser doping played an important role in control of defect formation, and they minimized the laser doping induced defects through applying a double  $\text{SiO}_2/\text{SiN}_x$  stack. Ohmer *et al.*<sup>21</sup> suggested that the laser beam with a line focus could help to avoid the formation of dislocations, microtwins, and phase changes in laser doping. Abbott *et al.*<sup>10</sup> and Baumann *et al.*<sup>26</sup> claimed that the laser-groove formation could induce less defects and device degradation in buried contact solar cells. Other studies<sup>14</sup> mainly evaluated the bulk carrier lifetime after the laser treatment. To further advance the understanding of laser-induced defects, this work focuses on the evaluation of laser-induced defect types and origins, defect energy levels, defect concentrations, and their influences on degradation of electrical properties and device performance.

The degradation of electrical properties due to laser-induced defects include carrier lifetime ( $\tau$ ),<sup>9,10,14,16</sup> leakage current ( $J_R$ ),<sup>11,13,16</sup> drift mobility ( $\mu$ ), and conductivity ( $\sigma$ ). The average carrier diffusion length is determined by the product of  $\mu\tau$ . First, the minority carrier lifetime ( $\tau$ ) can provide the time limit for the carrier recombination process. Next, the reverse leakage current ( $J_R$ ) can indirectly determine the recombination process and it has a correlation with minority carrier lifetime ( $\tau$ ). The carrier recombination in silicon (indirect bandgap) highly depends on the defect level, so the defect-induced recombination sites become the major source of leakage current in a junction. On the other hand, the drift mobility ( $\mu$ ) depends on the carrier transport and scattering process through  $\mu = e\tau_{\text{scattering}}/m$ , where  $\tau_{\text{scattering}}$  is the scattering time,  $e$  is carrier charge, and  $m$  is the effective mass; and the conductivity ( $\sigma$ ) is proportional to the drift mobility ( $\mu$ ) as expressed by  $\sigma = ne\mu$ , where  $n$  is the carrier concentration. It is noted that conductivity and mobility have not been investigated in single-crystalline silicon solar cells, which is most likely due to the sufficiently high mobility and conductivity of single crystalline phase. However, the laser-induced phase transformation to amorphous and polycrystalline phases<sup>24</sup> brings new interest in assessing the surface drift mobility and conductivity after laser processing.

In this work, we identified the induced defect types at different laser fluence regimes, analyzed the origins of laser-induced dislocations and strain, and assessed their magnitude in Sec. III. Moreover, we evaluated the impact of laser-induced defects on the carrier recombination and charge transport in the silicon surface in Sec. IV. In particular, we quantitatively correlated the laser-induced defects with the measured surface carrier lifetime, surface drift mobility,

surface conductivity, and leakage current at various laser fluences. Finally, we demonstrated the control of induced defects in laser-processed silicon solar cells through post furnace or laser annealing in Sec. V.

## II. EXPERIMENTAL DETAILS

### A. Laser processing of crystalline silicon

Polished p-type (boron-doped) FZ c-Si wafers were used, with a thickness of  $300\ \mu\text{m}$ , an orientation of  $\langle 100 \rangle$ , and a resistivity of  $1\ \Omega\ \text{cm}$ . They were purchased from Topsil Global Wafers. Wafers were cleaned by a standard procedure<sup>5,8</sup> to remove any organics, oxides, and metal ion contaminations.

Laser processing on the silicon wafer was conducted with a 30 W, 1064 nm pulsed fiber laser (model YLP-RA-1/50/30/30, IPG Photonics) with a laser pulse width of 50 ns. As shown in Fig. 1(a), the laser beam entered a galvanometer scanner (TS8310) and was scanned onto the wafer surface with the beam size focused to  $\sim 60\ \mu\text{m}$ . The laser repetition rate was set at 30 kHz, the scanning speed at 50 mm/s, and the line spacing at  $20\ \mu\text{m}$ , which guaranteed that the entire  $2\ \text{cm} \times 2\ \text{cm}$  sample surface was uniformly processed.

The laser fluences were varied ranging from 0.18 to  $1.92\ \text{J}/\text{cm}^2$  with a step of 0.02–0.2  $\text{J}/\text{cm}^2$ . The laser marking (ablation) on the silicon surface started at  $1.28\ \text{J}/\text{cm}^2$  fluence, while the laser melting occurred at  $\sim 0.4\ \text{J}/\text{cm}^2$ . Thus, the designed laser conditions covered three distinctive regimes: below laser melting, between laser melting and ablation, and above laser ablation.

### B. Characterization and quantification of laser-induced surface defects

The laser-induced defect generation was investigated by studying the band-edge and dislocation-induced photoluminescence emission. The induced dislocation concentration was quantified by observing etch pits under a scanning electron microscope (SEM), the induced strain was analyzed through X-ray diffraction (XRD), and the oxygen incorporation was detected using cross-sectional energy-dispersive X-ray spectroscopy (EDS) under transmission electron microscopy (TEM). The induced phase changes,<sup>24</sup> microtwins,<sup>24</sup> and point defects<sup>27</sup> are reported in separate papers.

#### 1. Photoluminescence

To reveal the surface defect information using photoluminescence, a 532 nm wavelength laser (DPSS, Melles Griot) was chosen as the excitation source. This 532 nm laser

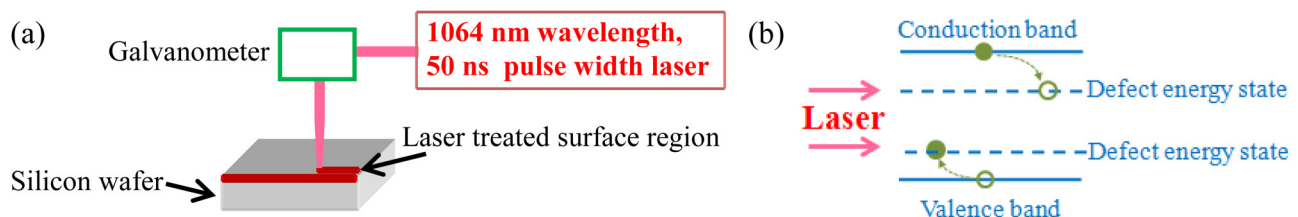


FIG. 1. (a) Schematic of laser processing of silicon surface and (b) generation of defect energy level in the silicon bandgap.

has a smaller penetration depth ( $\sim 1\ \mu\text{m}$ ) than the laser used for processing silicon. The continuous-wave laser beam passed through an optical chopper (SR540) and changed into pulses with a frequency of 100 Hz. The pulsed beam was absorbed by the sample surface causing photoexcitation and photoluminescence. The photoluminescence signal was collected in the spectrometer (iHR 320) using an InGaAs photoreceiver. To improve the signal and reduce the noise, we implemented four strategies: a lock-in amplifier (SR 830 DSP) to amplify the excited photoluminescence signal; filtering of the photoluminescence light signal through the long-pass band and green-light (532 nm) filters; use of higher laser power (1.7 W, maximum power: 2.5 W) for a strong carrier excitation; and cooling of the photoreceiver at  $-40\ ^\circ\text{C}$ .

## 2. Dislocation density

To quantify the dislocation density, a dislocation etch-pit study was carried out. Isotropic etching using mixed hydrofluoric, nitric, and acetic acid ( $\text{HF}$ ,  $\text{HNO}_3$ , and  $\text{CH}_3\text{COOH}$ ) for 6 h made etch pits observable at the dislocation sites due to preferential etching under the intensive strain field around dislocations. A scanning electron microscope (SEM, FEI Quanta 650) was used to observe the etch pits. The dislocation density  $D$  was determined by  $D = \frac{N}{A}$ , where  $N$  is the number of etch pits and  $A$  is the total area used for counting.

## 3. Internal strain

The internal strain was evaluated using an X-ray diffractometer (XRD, PANalytical X'Pert PRO MRD). The angular step size was set to  $0.002^\circ$  for achieving a high resolution. Laser-induced strain led to a lattice spacing change, thus the diffraction angle (peak position) shifted according to Bragg's law. After that, laser-induced strain was determined by

$$\varepsilon = \frac{d_{\text{laser}} - d_0}{d_0} = -\cot \theta_0 (\theta_{\text{laser}} - \theta_0), \quad (1)$$

where  $\varepsilon$  is the laser-induced strain,  $d_{\text{laser}}$  and  $\theta_{\text{laser}}$  are the spacing of lattice planes and diffraction angle in the laser-processed sample, respectively, and  $d_0$  and  $\theta_0$  are the spacing of lattice planes and diffraction angle in the reference sample without any laser processing, respectively.<sup>28</sup>

## 4. Oxygen incorporation

In order to detect the surface oxygen composition, the sample cross section was examined using energy-dispersive X-ray spectroscopy (EDS), which was incorporated into transmission electron microscopy (TEM, JEOL 2000FX). To prepare cross-sectional TEM samples for surface EDS, the laser-processed and non-laser-processed silicon samples were manually polished down to  $\sim 50\ \mu\text{m}$  via sandpapers. Then, the samples were ion-milled to 10–50 nm using a GATAN 691 Precision Ion Polishing System (PIPS). The thickness was monitored via a Zygo optical profilometer. A TEM aperture was placed on the surface (laser processed) region to achieve the EDS surface detection.

## C. Surface analysis of electrical properties after laser processing

The laser-defect induced degradation of surface electrical properties was evaluated by measuring surface carrier lifetime using near-surface photoconductance decay (ns-PCD), surface drift mobility and conductivity using the charge extraction by linearly increasing voltage (CELIV) method, and surface leakage current using dark I-V curves of dual Schottky barriers.

### 1. Surface charge carrier lifetime

The surface carrier lifetime was determined by a near-surface photoconductance decay (ns-PCD) method described by Drummond *et al.*<sup>29</sup> In the measurement, excess carriers were injected on the silicon surface by a pulsed laser beam, allowing the detection of surface carrier decay time.

### 2. Surface drift mobility and conductivity

The surface drift mobility and conductivity were measured using a charge extraction by linearly increasing voltage (CELIV) method.<sup>30</sup> A linearly increasing voltage was applied to a Schottky junction (Al-Si). The electrical field can charge the capacitor-like junction and the current density saturated at a certain time ( $t_{\text{max}}$ ). Afterward, due to carrier drifting, the extracted current density dropped back to the equilibrium level. Through the saturation time ( $t_{\text{max}}$ ), the carrier drift mobility ( $\mu$ ) was determined by

$$\mu = \frac{2d^2}{3At_{\text{max}}^2 K}, \quad (2)$$

where  $d$  is the distance of two contacts,  $A$  is the contact area, and  $K$  is a correction factor.<sup>30</sup> Also, the surface conductivity was calculated by

$$\sigma = \frac{3\varepsilon_0\varepsilon_r\Delta j}{2t_{\text{max}}j(0)}, \quad (3)$$

where  $\varepsilon_0$  is the permittivity of vacuum,  $\varepsilon_r$  is the relative permittivity of silicon,  $\Delta j$  is the difference of current density during carrier extraction, and  $j(0)$  is the starting current density.<sup>30</sup>

As a reference, the starting wafer's hole mobility was measured using a Hall Effect measurement system (ECOPIA HMS-3000).

### 3. Leakage current

The leakage current was measured through the dark I-V curves. Two 500 nm thick aluminum contacts with a diameter of 2 mm were deposited on the laser-processed silicon surface to create dual Schottky barriers. The nearest distance between two contacts was  $215\ \mu\text{m}$ . Two probes were placed on the two aluminum contacts (nominally in the center region), respectively. A Keithley 2400-C source meter was connected with the probes and used to generate the I-V curves. Under either forward or reverse voltage, only the leakage current can travel through the device.

### D. Furnace or laser annealing of laser-processed silicon solar cells

The laser-processed silicon interdigitated back contact (IBC) solar cells (active area =  $1 \text{ cm}^2$ ) were fabricated to assess the furnace or laser annealing of induced defects. The furnace annealing was conducted at  $800^\circ\text{C}$  for 30 min using a tube furnace (MRL Industries).

The laser annealing was carried out using a 150 W, 1070 nm wavelength pulsed ytterbium fiber laser system (model YLR-150/1500-QCW-AC, IPG Photonics) with a pulse width of  $300 \mu\text{s}$ . The laser beam was focused to a spot size of 3.2 mm and was operated at a repetition rate of 500 Hz. A galvanometer scanner with a scan speed of 600 mm/s was used to achieve area annealing on the sample. The laser fluence was fixed at  $0.38 \text{ J/cm}^2$  to anneal all laser-processed samples.

The laser-processed silicon solar cell fabrication steps include (a) chemical microtexturing, (b) emitter doping and back surface field formation by laser doping, (c) furnace or laser annealing for removal of laser-doping induced defects, (d) surface passivation with 15 nm thermal oxide and 70 nm PECVD silicon nitride, (e) metal contact formation for n and p regions by a laser transfer method, (f) a second furnace or laser annealing for removal of induced defects from laser-transferred metal contacts, (g) electroplating, and (h) forming gas annealing (FGA) at  $400^\circ\text{C}$  for 15 min. Further details on the device fabrication steps and characterization can be found in Refs. 4 and 15.

### III. LASER-INDUCED DEFECT GENERATION

#### A. Laser-induced defect types using band-edge and dislocation-induced photoluminescence

The band-edge photoluminescence emission can determine the overall effect of laser-induced defects on the crystal

quality, and the dislocation-induced photoluminescence can directly indicate the influence from dislocations. The band-edge photoluminescence arose from the radiative recombination under the input photons. If laser-induced dislocations existed, the excited carriers would recombine at the dislocation energy state [Fig. 1(b)], inducing the dislocation photoluminescence.

Figure 2(a) shows the band-edge photoluminescence evolution with increasing laser fluences. We observed the main photoluminescence peak at 1.06 eV, which is slightly lower than the 1.1 eV bandgap energy. This 0.04 eV shift toward a low energy level is due to the boron doping.<sup>31</sup> To reveal the laser fluence dependence, the maximum band-edge photoluminescence intensities were quantified as a function of laser fluence as shown in Fig. 2(b). Two sets of samples were studied to ensure the repeatability.

The photoluminescence data [Fig. 2(b)] suggest three stages of laser-silicon interactions. First, the band-edge photoluminescence intensity increased in a low fluence regime ( $0.3\text{--}0.4 \text{ J/cm}^2$ ). This behavior is most likely due to the annealing of pre-existing defects (dislocation density:  $1 \times 10^6 \text{ cm}^{-2}$ ) in the starting wafer, and the capability of laser annealing at  $0.3\text{--}0.4 \text{ J/cm}^2$  fluences to remove defects has been demonstrated in our previous work.<sup>8</sup> With slightly increased laser fluence ( $0.4\text{--}0.5 \text{ J/cm}^2$ ), an immediate but small decrease of the intensity was observed. This is highly likely due to the melting of silicon with the generation of resolidification-induced point defects,<sup>27</sup> or due to the accumulated defects by sub-melting threshold irradiation with multiple pulses. In the literature,<sup>32,33</sup> it was reported that defects could accumulate in Si with multiple pulses that were well below the melting threshold. However, the nature of multiple-pulse-induced defects below the melting threshold is not clear yet.<sup>32</sup> It is possible that some accumulated defects were produced by sub-melting threshold irradiation

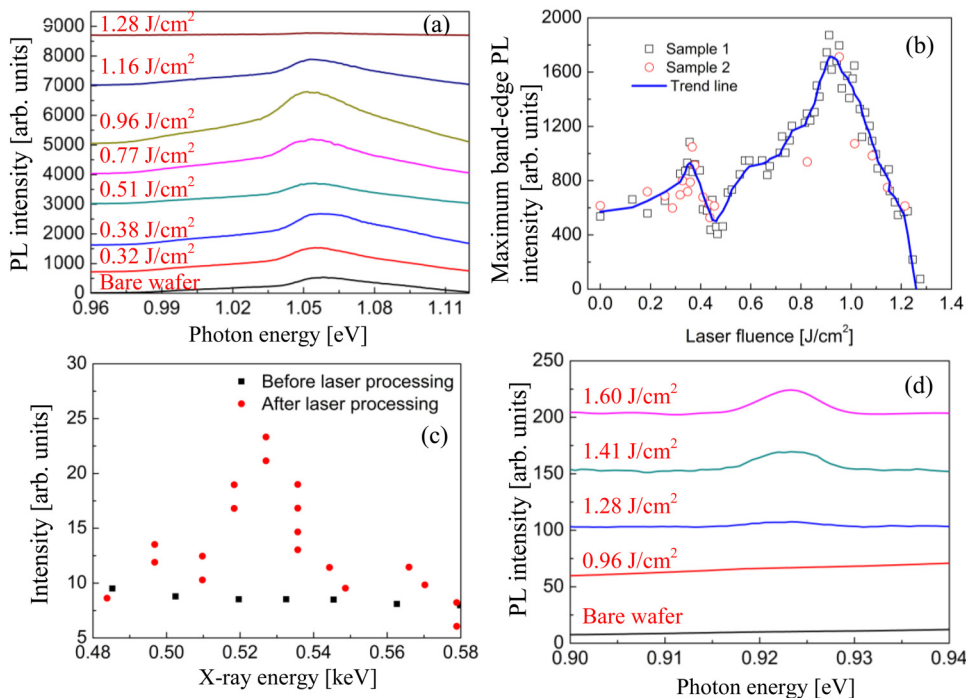


FIG. 2. (a) Band-edge photoluminescence (PL) spectra with increasing laser fluences. (b) Maximum intensity of band-edge photoluminescence peak as a function of laser fluence. (c) EDS spectra of oxygen element on the silicon cross section measured under TEM before and after laser processing. (d) Dislocation-induced photoluminescence spectra with increasing laser fluences.



but they were not observed by photoluminescence. Note that little amount of degradation of electrical material parameters (carrier lifetime, drift mobility, and conductivity) was observed below the melting threshold, which also indicates the existence of some non-observed defects from sub-melting threshold irradiation.

In the second stage, after the laser fluence was further increased from  $0.5 \text{ J/cm}^2$  to  $1 \text{ J/cm}^2$ , a distinctive enhancement of band-edge photoluminescence was observed, which is highly likely due to the oxygen incorporation. At this laser fluence range, between laser melting and ablation, the surface of single-crystalline silicon wafers most likely became amorphized.<sup>24</sup> The oxygen atoms were reported to diffuse rapidly in laser-induced amorphous silicon.<sup>34</sup> Using EDS under TEM, we found that oxygen elements only appeared in the laser-processed region as shown in Fig. 2(c), which confirmed the oxygen incorporation during laser processing. The incorporated oxygen existed in the form of Si-O complexes,<sup>34</sup> and they can greatly improve the Si band-edge photoluminescence, since the indirect bandgap of silicon yields photoluminescence requiring the phonon assistance such as so-called oxygen thermal donors.<sup>35</sup>

In the final stage, after the laser fluence was increased above  $1 \text{ J/cm}^2$ , the band-edge photoluminescence dropped dramatically. At this laser fluence range, the laser ablation started, which was confirmed by the observation of ablated spot on the silicon surface at  $1.28 \text{ J/cm}^2$ . The laser ablation process could break down the Si-O bonds and also generate dislocations, resulting in a significant loss of band-edge photoluminescence. Above  $1.28 \text{ J/cm}^2$  laser fluence, the band-edge photoluminescence disappeared, suggesting that large numbers of dislocations led to carrier recombination at the dislocation energy states.

The direct evidence of laser-induced dislocation generation can be obtained from dislocation-induced photoluminescence spectra as shown in Fig. 2(d). The dislocation-induced photoluminescence at  $0.924 \text{ eV}$  energy appeared at the  $1.28 \text{ J/cm}^2$  laser fluence, which explains the complete loss of band-edge photoluminescence. The identified energy level at  $0.924 \text{ eV}$  for laser-induced dislocations matches with the so-called D3 line at  $0.92 \text{ eV}$  among possible dislocation energy states in silicon.<sup>36</sup> The dislocation peak became prominent at  $1.41 \text{ J/cm}^2$  and  $1.60 \text{ J/cm}^2$  fluences, suggesting an increasing dislocation density with laser fluence (Sec. III B).

In summary, the laser-induced defect types with increasing laser fluences are revealed. Below the laser melting, defects are removed due to the annealing effect;<sup>8</sup> and no defects are identified although very little degradation of electrical properties is observed. Between the laser melting and laser ablation, the point defect generation occurs including vacancies,<sup>27</sup> self-interstitials,<sup>27</sup> and impurity atoms; more importantly, the oxygen incorporation (a kind of point defects) becomes significant; also, the amorphous phase is generated.<sup>24</sup> Above the laser ablation, dislocations are notably observed with the generated strain (Sec. III C); also, grain boundaries (polycrystalline phase) and microtwins are generated.<sup>24</sup> This summary can provide directions for steering and manipulating certain or all types of induced defects during laser processing of silicon semiconductor.

## B. Quantification of dislocation density with increasing laser fluences

The dislocation density was determined by the etch pit density, and the data are shown in Fig. 3(a). The  $1.28 \text{ J/cm}^2$ -fluence processed sample showed very limited etch pits, and its dislocation density was  $2.17 \times 10^6 \text{ cm}^{-2}$ ,

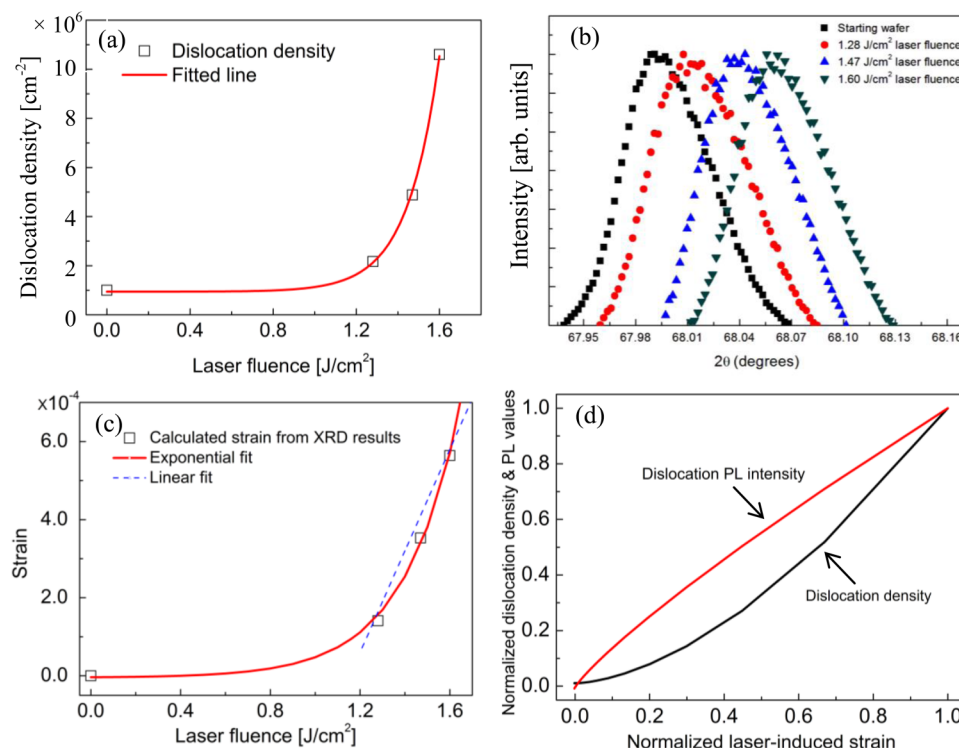


FIG. 3. (a) Dislocation density with increasing laser fluence. (b) XRD patterns after laser processing under different fluences. (c) Calculated strain from XRD results plotted against laser fluence. (d) Normalized laser-induced dislocation density and dislocation-induced photoluminescence (PL) intensity variation as a function of laser-induced strain, showing the origin of laser-induced dislocation formation.

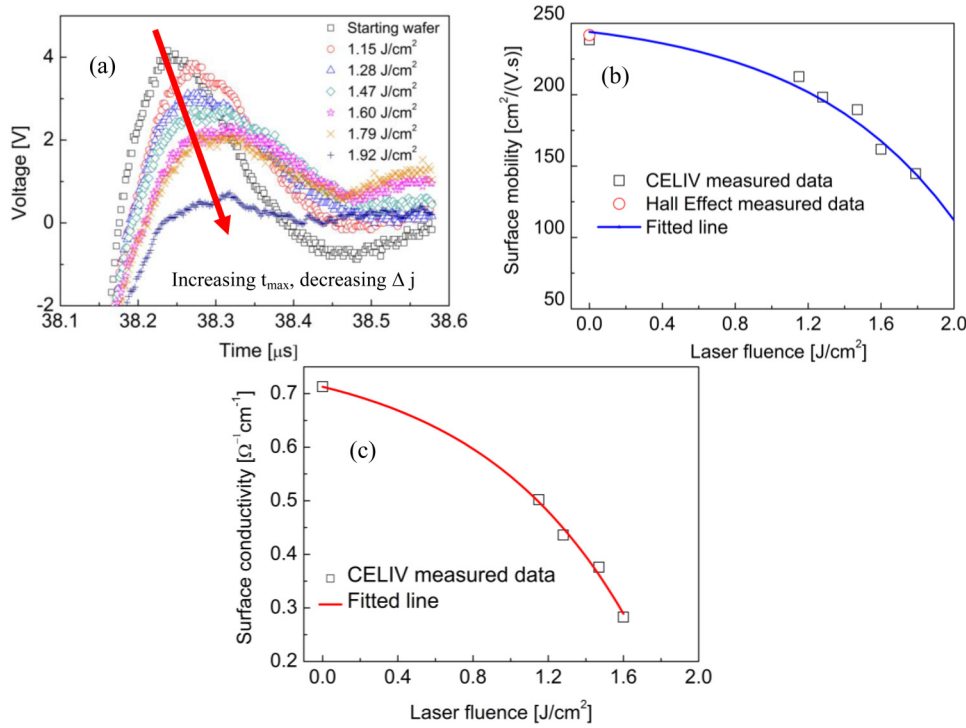


FIG. 4. (a) CELIV (charge extraction by linearly increasing voltage) curves at various laser fluences. (b) Surface drift mobility and (c) surface conductivity as a function of laser fluence. The data were extracted from the CELIV measurements, and the drift mobility data of starting wafers were calibrated using Hall Effect measurement.

which is a very small value as compared to the  $1 \times 10^6 \text{ cm}^{-2}$  density in the starting wafer. Above  $1.28 \text{ J/cm}^2$  laser fluence, the dislocation density increased dramatically. The trend was fitted exponentially and the relationship could be expressed by

$$D = 280 \exp\left(\frac{F}{0.15}\right) + 9.39 \times 10^5, \quad (4)$$

where  $D$  is the laser-induced dislocation density and  $F$  is the laser fluence. The reason of exponential fitting is that the possible origin of dislocations, the laser-induced strain, follows a probable exponential increase with laser fluence as discussed in Sec. III C. Note that the quantified data match with our photoluminescence results, which confirms the data validity and suggests the potential use of photoluminescence as a non-destructive technique for monitoring laser-induced dislocation density.

### C. Origin of laser-induced dislocations and laser-induced strain

Based on the literature,<sup>22,38</sup> the formation mechanisms of dislocation generation in laser processed silicon are discussed. During laser-silicon interaction, electrons are excited owing to laser energy absorption, and the material turns into the plasma state.<sup>37</sup> Plasma contains ions and electrons. The plasma could have high frequency vibrations.<sup>38</sup> Due to a non-equilibrium laser process, the collisions of ions in the plasma are capable of the displacement of atoms (dislocations or point defects) during the lattice formation.<sup>39</sup> The laser ablation process was highly likely to enhance the collisions of ions in the plasma. This explains how the two-dimensional displacement of atoms (dislocations) was preferably generated after laser ablation.

Moreover, laser-induced strain can contribute to the dislocation generation during laser processing.<sup>22</sup> The displacement of atoms from collisions of ions in the plasma results in the generation of point defects and dislocations. These defects can include additional strain in addition to the thermal strain. Additionally, the oxygen incorporation can affect the dislocation movement.<sup>40</sup>

Since the internal strain field is a major origin and indicator of dislocation generation, the change of internal strain field after laser processing was investigated and quantified by studying XRD patterns of silicon peaks. As shown in Fig. 3(b), the silicon peak had an increase in the Bragg diffraction angle after laser processing. This increase is due to the expansion strain generated by laser processing. The induced strain was quantified based on Eq. (1). The calculated strain was plotted against increasing laser fluence as shown in Fig. 3(c). To effectively fit the trend, we compared the exponential and linear fitting. The exponential fitting showed a low error; thus, the exponential relationship was cautiously adopted for the induced strain study and applied to the fitting for the resulting dislocation density and degradation of surface electrical properties. Note that the exponential relationship may be only true within the laser fluences studied ( $0\text{--}2 \text{ J/cm}^2$ ), which are typically used for laser processing of silicon solar cells.

The laser-induced strain ( $\epsilon$ ) with increasing fluence ( $F$ ) could be expressed by

$$\epsilon = 9.56 \times 10^{-7} \exp\left(\frac{F}{0.25}\right) - 4.6 \times 10^{-6}. \quad (5)$$

Based on this equation, the strain in the starting wafer is  $3.64 \times 10^{-6}$ , which is on the same magnitude of the reported  $6 \times 10^{-6}$  value.<sup>41</sup> At  $1.28 \text{ J/cm}^2$  laser fluence, the strain increased to  $1.41 \times 10^{-4}$ . Above  $1.28 \text{ J/cm}^2$  fluence, the strain

increased significantly. This trend matches with the increase of laser-induced dislocation density and dislocation-induced photoluminescence. As shown in Fig. 3(d), after normalization, the dislocation-related values are roughly in a linear relationship with laser-induced strain, which demonstrates the induced strain from laser nonequilibrium thermodynamics is a possible major source of induced dislocations.

#### IV. LASER-INDUCED DEGRADATION OF SURFACE ELECTRICAL PROPERTIES

##### A. Degradation of surface drift mobility and conductivity

The surface drift mobility and conductivity are the direct parameters to evaluate carrier transport properties after laser processing. Their dependencies on laser fluences were measured using an equilibrium charge extraction by linearly increasing voltage (CELIV) method. Figure 4(a) shows that the current saturation time ( $T_{\max}$ ) increased with laser fluence, indicating decreased surface drift mobility. Moreover, the extracted current density ( $\Delta j$ ) decreased with increasing laser fluence, which suggests a decreased surface conductivity due to defect-assisted scattering and recombination of carriers.

The extracted surface drift mobilities from CELIV measurements are shown in Fig. 4(b). The starting wafer showed a mobility of  $238.4 \text{ cm}^2/(\text{V s})$ , and this value matches with the measured Hall mobility of  $241.7 \text{ cm}^2/(\text{V s})$ , which confirms the data validity. With increasing laser fluence ( $F$ ), the surface drift mobility ( $\mu$ ) dropped nearly exponentially and the trend was fit by

$$\mu = -13 \exp\left(\frac{F}{0.83}\right) + 257. \quad (6)$$

The exponential drop is possibly because the dislocation density increases roughly exponentially with laser fluence [Fig. 3(a)]. These induced defects played two roles: scattering the carriers during their movement and providing the recombination sites, which lowered the drift mobilities.

Similarly, the extracted surface conductivity from CELIV measurements is shown in Fig. 4(c). The starting wafer showed a surface conductivity of  $0.71 \Omega^{-1} \text{ cm}^{-1}$  which matches with the manufacturer provided wafer resistivity of approximately  $1 \Omega \text{ cm}$ . The decreasing surface conductivity ( $\sigma$ ) after laser processing was also likely exponential and fitted using

$$\sigma = -0.07 \exp\left(\frac{F}{0.82}\right) + 0.783, \quad (7)$$

where  $F$  is the laser fluence. Since the conductivity is proportional to the drift mobility, the induced defects imposed a similar effect on the surface conductivity.

##### B. Degradation of surface carrier lifetime and leakage current

The carrier lifetime is the direct measure for evaluating defect-induced recombination after laser processing. The surface carrier lifetime was determined by near-surface photoconductance decay (ns-PCD). Figure 5(a) shows the degradation of surface carrier lifetime ( $\tau$ ) defined by a probable exponential relationship via

$$\tau = -150 \exp\left(\frac{F}{0.87}\right) + 1390, \quad (8)$$

where  $F$  is the laser fluence. The carrier lifetime was reported to affect the open circuit voltage ( $V_{oc}$ ) in a logarithmic relationship,<sup>42</sup> which suggests that the increasing laser-

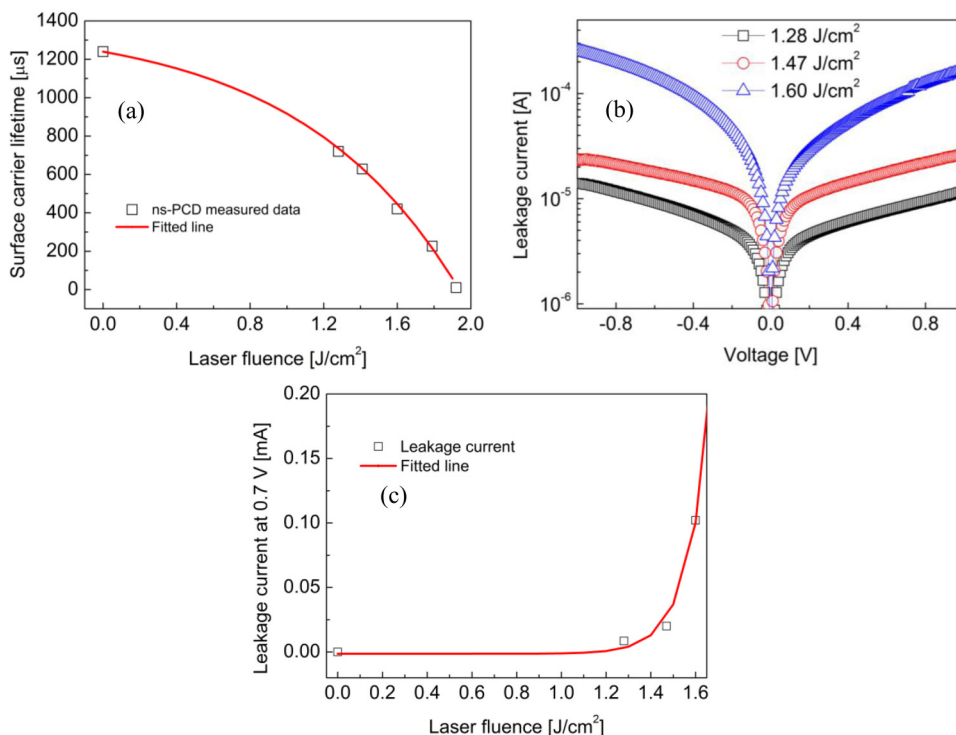


FIG. 5. (a) Surface carrier lifetime as a function of laser fluence. (b) Leakage current after laser processing under various fluences and (c) the leakage current at 0.7 V plotted against laser fluence.

processing fluence ( $0.4\text{--}2\text{ J/cm}^2$ ) would degrade the open circuit voltage of Si solar devices roughly in a linear relationship.

The leakage current can reveal the influences from induced defects on the junction. To measure the leakage current, we created a simple device structure with two 2 mm diameter Al contacts on the p-type Si surface. The calculated junction barrier height between Al contact and p-type Si wafer is 0.85 eV. The leakage current can be observed only when the defect energy level exists within the Si bandgap, which provides the leakage channel in the junction. The dark current-voltage curves showing the leakage current under various laser processing fluences are shown in Fig. 5(b). As shown, the magnitude of leakage current increased from  $10^{-5}$  A to  $10^{-4}$  A, after the laser fluence increased from  $1.28\text{ J/cm}^2$  to  $1.60\text{ J/cm}^2$ . The leakage current at 0.7 V for various laser fluences was fitted to a probable exponential relationship as shown in Fig. 5(c). Interestingly, the increase of leakage current at  $0.4\text{--}1\text{ J/cm}^2$  laser fluences is not as much as the degradation of other surface electrical properties [Figs. 4(b), 4(c), and 5(a)]. At this laser fluence regime, laser-induced point defects are the major defect type; but the point-defect energy states do not likely satisfy the junction barrier requirement for current leakage, which explains the degradation difference.

### C. Effect of laser-induced defects on surface electrical properties

In order to reveal the influences of laser-induced defects on surface electrical properties, the relative values for surface carrier lifetime, surface drift mobility, and surface conductivity are plotted as a function of laser-induced dislocation density based on Eqs. (4) and (6)–(8).

As shown in Fig. 6, the degradation of surface electrical properties is below 20% when the laser-induced dislocation density is around  $10^6\text{ cm}^{-2}$ . Above  $10^6\text{ cm}^{-2}$ , all three surface electrical parameters degrade quickly. According to the laser-induced dislocation density versus the laser fluence data [Fig. 3(a)], the laser-processing fluence should be chosen near the Si melting regime in order to minimize the

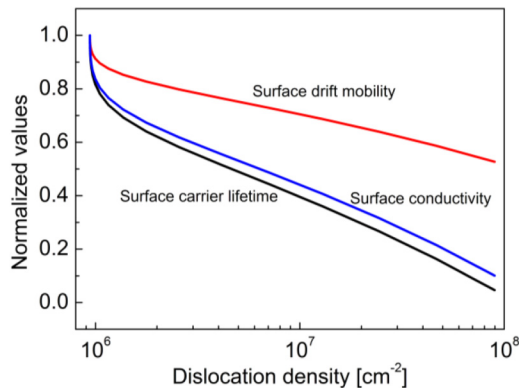


FIG. 6. Surface electrical properties of laser-processed silicon as a function of induced dislocation density: surface carrier lifetime, surface drift mobility, and surface conductivity.

induced dislocation density and surface property degradation during laser processing of Si solar cells.

To determine the critical limits of surface electrical properties for achieving 20.5% efficient Si solar cells (state-of-the-art of industrial solar cells<sup>43</sup>), we discuss the various loss mechanisms in controlling device performance as summarized in Table I. The surface carrier lifetime ( $\tau$ ) is directly related to the carrier recombination process and mainly affects the open circuit voltage through  $V_{oc} = \frac{2kT}{q} \ln\left(\frac{J_{sc} \times \tau}{q n_i W}\right)$ ,<sup>44</sup> where  $J_{sc}$  is the short circuit current density,  $W$  is the wafer thickness,  $n_i$  is the intrinsic carrier density of silicon,  $k$  is the Boltzmann constant,  $q$  is the electronic charge, and  $T$  is the temperature. Based on achieving  $V_{oc}$  of 0.66 V,  $J_{sc}$  of  $39.19\text{ mA/cm}^2$ , and wafer thickness of  $200\text{ }\mu\text{m}$  for 20.5% efficiency,<sup>43</sup> the carrier lifetime limit is identified to be  $236\text{ }\mu\text{s}$ . This value suggests, for a starting 1.2-ms-lifetime silicon wafer, 80% degradation of carrier lifetime and  $5 \times 10^7\text{ cm}^{-2}$  dislocation density are acceptable in the laser-processed solar cells and still 20.5% efficient cells could be achieved. Note that this tolerated degradation limit is only true when a recombination mechanism is considered in terms of laser-induced defects, and there are other recombination mechanisms such as metal and emitter interface.

The surface drift mobility ( $\mu$ ) is directly related to the carrier scattering process and would affect the short circuit current ( $I_{sc}$ ) when the carrier lifetime is low.<sup>45</sup> According to the literature,<sup>45</sup> the mobility limit is  $\sim 24\text{ cm}^2/(\text{V s})$  to achieve 20.5% photovoltaic efficiency using a  $100\text{-}\mu\text{s}$ -lifetime silicon wafer. This limit allows 90% degradation of surface mobility after laser processing, and a higher efficiency can be easily attained through improving the  $\mu\tau$  product.

The surface conductivity ( $\sigma$ ) determines the series resistance ( $R_s$ ) and would affect the fill factor (FF) through  $FF = \frac{I_m R_s}{V_{oc} I_{sc}}$ , where  $I_m$  is the maximum photovoltaic current. The required series resistance ( $R_s$ ) in the 20.5% efficient cell is  $2.257\text{ m}\Omega$ .<sup>43</sup> If it is assumed that the resistance of laser-processed surface region ( $R_{surf}$ ) and the resistance of bulk region ( $R_{bulk}$ ) are connected in series, the equivalent series resistance would be  $R_s = R_{surf} + R_{bulk} = \frac{L_{surf}}{\sigma_{surf} A} + \frac{L_{base} - L_{surf}}{\sigma_{base} A}$ , where wafer thickness ( $L_{base}$ ) is close to  $200\text{ }\mu\text{m}$  and area  $A$  is  $242\text{ cm}^2$  used in the 20.5% efficient cell.<sup>43</sup> The bulk conductivity of the starting wafer is  $0.71\text{ }\Omega^{-1}\text{ cm}^{-1}$ , and laser-

TABLE I. Critical limits of surface electrical properties for achieving 20.5% efficient solar cells ( $V_{oc} = 0.66\text{ V}$ ,  $J_{sc} = 39.19\text{ mA/cm}^2$ ,  $R_s = 0.009\text{ m}\Omega/\text{cm}^2$ , wafer thickness =  $200\text{ }\mu\text{m}$ ).

Surface electrical properties	Minimum values	Starting wafer values	Acceptable degradation (%)	Allowed dislocation density ( $\text{cm}^{-2}$ )
Carrier lifetime ( $\mu\text{s}$ )	236	1240	80	$5 \times 10^7$
Drift mobility [ $\text{cm}^2/(\text{V s})$ ]	24	238	90	$> 10^8$
Conductivity ( $\Omega^{-1}\text{ cm}^{-1}$ )	0.002	0.71	99.7	$\sim 10^8$



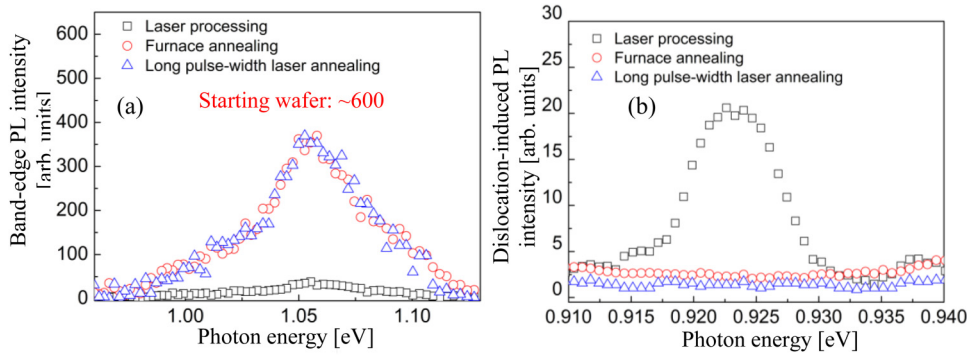


FIG. 7. (a) Band-edge photoluminescence (PL) and (b) dislocation-induced photoluminescence spectra after furnace or long-pulse-width (300  $\mu$ s) laser annealing of 1.28 J/cm<sup>2</sup>-fluence processed silicon.

heated depth is  $\sim 10 \mu\text{m}$  based on the modeling result.<sup>19</sup> Thus, the surface conductivity limit is  $0.002 \Omega^{-1} \text{cm}^{-1}$ , which allows 99.7% degradation of surface conductivity after laser processing. Note that this calculation does not take into account the contact resistance between the metal contact and the silicon wafer and also the resistance of metal contacts, the latter of which is very small.

## V. LASER AND FURNACE ANNEALING TO MINIMIZE LASER-INDUCED DEFECTS

The control of laser-induced defects can be achieved through two approaches: minimization of their generation by proper choice of laser-processing parameters and post laser or furnace annealing of the induced defects.<sup>8</sup> We investigated the furnace and long pulse-width laser annealing approaches to mitigate the induced defects in laser-processed silicon solar cell devices.

First, the effect of laser and furnace annealing of surface defects on 1.28-J/cm<sup>2</sup>-laser-fluence processed silicon semiconductor surface was demonstrated using photoluminescence as shown in Fig. 7. After furnace annealing at 800  $^{\circ}\text{C}$  for 30 min or long pulse-width (300  $\mu\text{s}$ ) laser annealing at 0.38 J/cm<sup>2</sup> fluence, the band-edge photoluminescence intensities [Fig. 7(a)] were recovered to  $\sim 400$  from the original value of  $\sim 50$  in the laser-processed samples, while the

dislocation-induced peak at 0.924 eV [Fig. 7(b)] disappeared. These data suggest that the laser-induced dislocations can be completely eliminated using either furnace or long pulse-width laser annealing. However, the band-edge photoluminescence did not recover to the value of  $\sim 600$  in the starting wafer, which indicates the amorphous/polycrystalline phase generation.<sup>24</sup>

Furthermore, we fabricated laser-processed silicon solar cells, and the device structure is shown in Fig. 8(a). In the fabrication process, two laser techniques, laser transfer doping and laser-transferred metal contacts, were used. As illustrated in Fig. 8(b), the laser transfer doping of aluminum created the p+ emitter doping region, while the laser transfer doping of phosphorus formed the n+ back surface field. Then, laser-transferred aluminum and titanium contacts were deposited on the p+ and n+ doped regions, respectively.

Additionally, the sheet resistance was measured to evaluate the laser annealing effect on laser-doped samples. As shown in Figs. 8(c) and 8(d), the sheet resistance of laser-doped phosphorus and aluminum samples both decreased after laser annealing. Especially, the sheet resistance of laser-doped phosphorus samples [Fig. 8(c)] dropped to  $\sim 50 \Omega/\square$  from the initial values of 100–230  $\Omega/\square$ . The decreased sheet resistance demonstrates an improved conductivity and mobility after laser annealing of laser-doped samples.

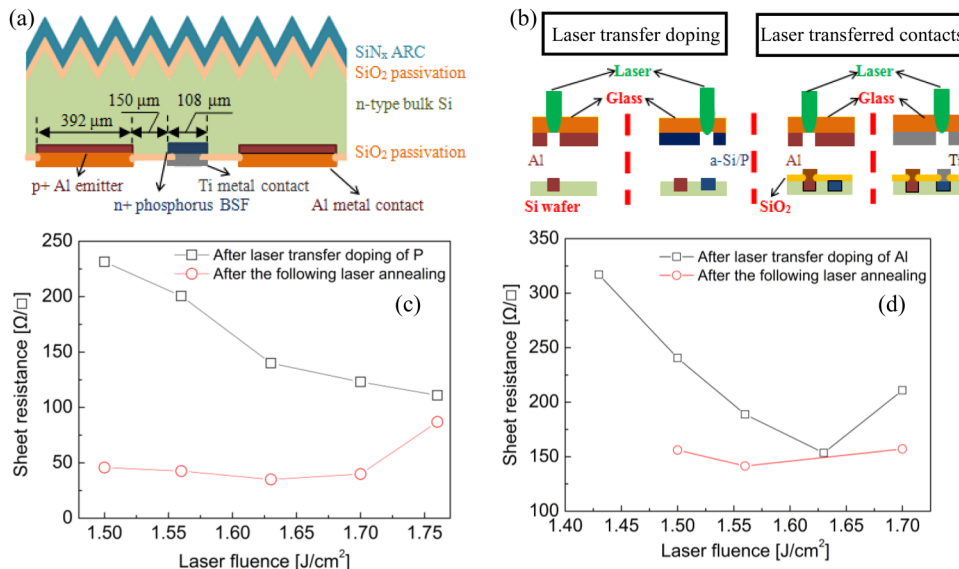


FIG. 8. (a) Laser-processed solar cell device structure. (b) Laser transfer doping of phosphorus (P) and aluminum (Al) for emitter doping and back surface field formation; and laser-transferred metal contacts of aluminum and titanium (Ti) for contact formation in p+ and n+ regions. (c)–(d) The sheet resistance of laser-doped (c) phosphorus and (d) aluminum samples, and their values after long pulse-width laser annealing.

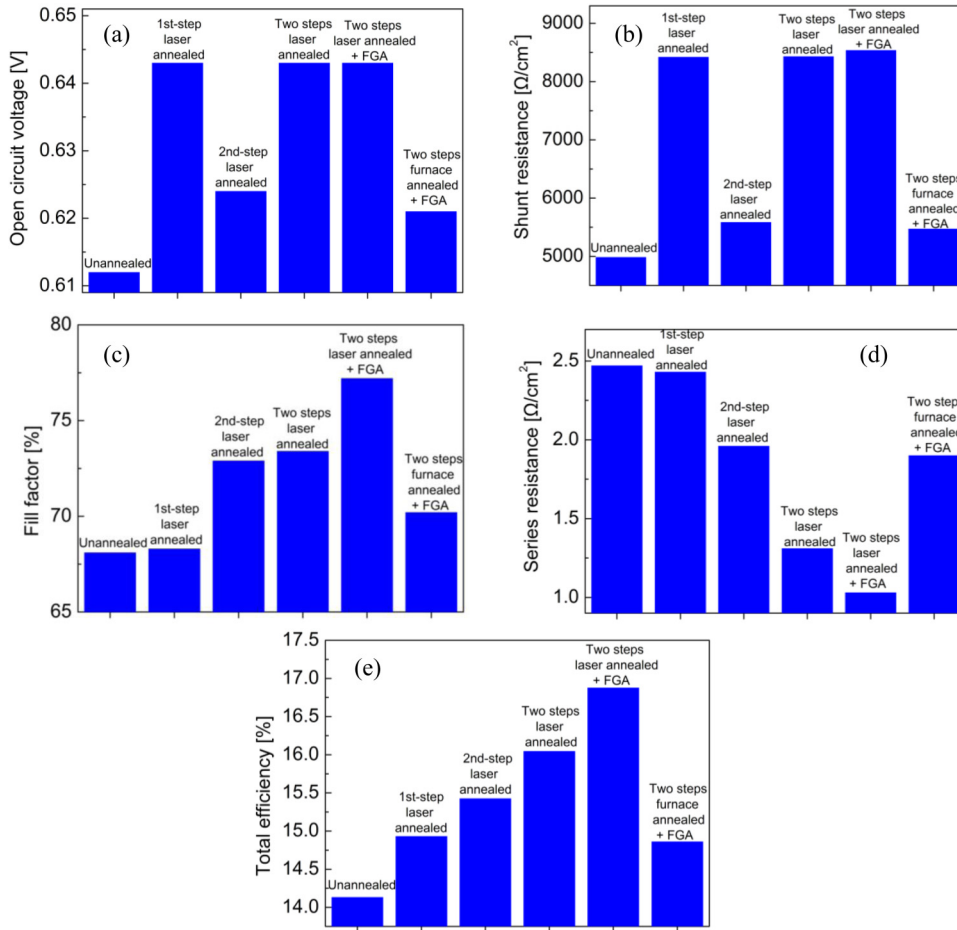


FIG. 9. (a) Open circuit voltage, (b) shunt resistance, (c) fill factor, (d) series resistance, and (e) total efficiency for (1) unannealed devices, (2) “1st step” laser-annealed devices with a single laser-annealing step after laser doping, (3) “2nd step” laser-annealed devices with a single laser-annealing step after laser-transferred metal contact formation, (4) two-step laser-annealed devices, (5) two-step laser-annealed and forming-gas-annealed devices, and (6) two-step furnace-annealed and forming-gas-annealed devices.

Finally, the device performance after laser and furnace annealing was evaluated as shown in Fig. 9. Two annealing steps were applied: the annealing after laser doping, denoted by “1st step” annealing, and the annealing after laser-transferred metal contacts, denoted by the “2nd step” annealing.

The laser-annealed devices with a single “1st step” annealing showed the increased open circuit voltage [ $V_{oc}$ , Fig. 9(a)] and higher shunt resistance [ $R_{sh}$ , Fig. 9(b)] as compared to the unannealed devices. The increased  $V_{oc}$  suggests that the “1st step” laser annealing can remove the defects induced by laser doping and decrease the carrier recombination near the junction. It is noted that laser doping involves the Si melting and could induce the defects near the junction.<sup>4</sup> This is consistent with the observation by Watkins<sup>32</sup> that significant degradation occurs in Si junction devices only when the laser melt front reaches the junction region. The recovery of the device performance achieved by the “1st step” laser annealing strongly indicates that this laser-annealing step is able to remove the critical defects near the junction. Moreover, as laser-induced defects were removed near the junction, the shunting channels were eliminated with the observed increase of shunt resistance. However, the  $V_{oc}$  and  $R_{sh}$  values were not further improved when the two-step laser annealing or additional forming gas annealing (FGA) were utilized, which suggests that the “1st step” laser annealing is the most critical step for the defect removal at the

junction where carriers require to be separated before recombination.

The laser-annealed devices with a single “2nd step” laser annealing showed the increased fill factors [FF, Fig. 9(c)] and decreased series resistance [ $R_s$ , Fig. 9(d)] as compared to the unannealed devices. The laser-transferred-contact process was optimized to gently deposit metal contacts on the silicon surface without affecting the silicon surface, and the laser-induced defects from this process were mainly at the silicon-metal interface. The decreased series resistance indicates that the “2nd step” laser annealing can remove the induced interface defects and improve the conductivity in the device. The  $R_s$  and FF values were further improved if additional forming gas annealing (FGA) was performed, since FGA can also decrease the contact resistance. With contributions from two-step laser annealing and additional forming gas annealing, the total efficiency showed a continuous improvement as shown in Fig. 9(e).

Finally, the laser and furnace annealing processes are compared. The furnace-annealed devices showed relatively poor performance. This is likely because the furnace annealing requires bulk processing and the defects would diffuse downward to the bulk region under a high temperature,<sup>46</sup> although the defects in the surface region were removed as indicated by the photoluminescence results [Fig. 7]. In contrast, the laser annealing is a surface processing technique, so the dislocations and point defects can diffuse out of the silicon surface.

## VI. CONCLUSIONS

The laser-induced defect types, origin of defects, and their concentration were determined using photoluminescence, X-ray, and etch pits. Below laser melting, very little degradation of electrical properties was observed, although no defects were identified. Above laser-ablation threshold, laser-induced dislocations were significantly generated, while the induced point-defects and oxygen incorporation were noticeably detected between laser melting and ablation thresholds. The laser-induced dislocation density and strain likely increased exponentially with laser fluence. The laser-induced strain was identified to be the possible major source of dislocation generation.

Moreover, the impact of laser-induced defects on surface electrical properties was evaluated using various surface characterization methods. The degradation of surface drift mobility, surface conductivity, surface carrier lifetime, and leakage current were governed by a probable exponential relationship with laser fluence, similar to dislocation generation. Through the loss analysis of device performance, a laser processing fluence near the Si melting regime was identified as the best value for minimizing laser-induced defects and degradation of surface electrical properties.

Finally, the control of laser-induced defects in laser-processed Si solar cell devices was demonstrated through post laser and furnace annealing. Through two-step laser annealing for removal of junction defects and silicon-metal interface defects, the open circuit voltage, fill factor, shunt resistance, and series resistance were considerably improved, resulting in an increased photovoltaic efficiency.

In summary, laser processing of silicon induces surface damage in terms of dislocations, points defect formation, and phase changes. These defects influence carrier lifetime, mobility, and hence conductivity and leakage current. This study provides the relationship between structural defects and electrical properties. In addition, this work demonstrates that structural defects can be significantly eliminated under laser annealing, allowing the suitability of a laser-processing method for high-efficiency low-cost silicon photovoltaic, microelectronic, and optoelectronic device fabrication.

## ACKNOWLEDGMENTS

The authors would like to acknowledge the support of the National Science Foundation (NSF) under Grant No. CMMI-1436775, the NASA Langley Professor Program, and the NSF I/UCRC award. The authors also extend their thanks to Professor Leonid V. Zhigilei and Miao He for valuable discussions about the results.

<sup>1</sup>C. Battaglia, A. Cuevas, and S. D. Wolf, "High-efficiency crystalline silicon solar cells: Status and perspectives," *Energy Environ. Sci.* **9**, 1552 (2016).

<sup>2</sup>M. Dahlinger, K. Carstens, E. Hoffmann, J. R. Kohler, R. Zapf-Gottwick, and J. H. Werner, "23.2% laser processed back contact solar cell: Fabrication, characterization and modeling," *Prog. Photovolt.* **25**, 192 (2017).

<sup>3</sup>B. K. Nayak, V. V. Iyengar, and M. C. Gupta, "Efficient light trapping in silicon solar cells by ultrafast-laser-induced self-assembled micro/nano structures," *Prog. Photovolt.* **19**, 631 (2011).

<sup>4</sup>Z. Sun and M. C. Gupta, "Laser annealing to enhance performance of all-laser-based silicon back contact solar cells," *Proceedings of the 44th IEEE PVSC* (IEEE, 2017), pp. 937–939.

<sup>5</sup>Z. Sun, X. Deng, J. J. Choi, and M. C. Gupta, "Silicon surface passivation by laser processing a sol-gel TiO<sub>x</sub> thin film," *ACS Appl. Energy Mater.* **1**, 5474–5481 (2018).

<sup>6</sup>L. Wang, D. E. Charlson, and M. C. Gupta, "Silicon solar cells based on all-laser-transferred contacts," *Prog. Photovolt.* **23**, 61 (2015).

<sup>7</sup>U. Das, C. Thompson, U. Nsofor, Z. Sun, M. C. Gupta, and S. S. Hegedus, "Effect of dielectric layers on laser-fired-contact performance in a-Si/c-Si heterojunction solar cells," *Proceedings of the 7th WCPEC* (IEEE, 2018).

<sup>8</sup>Z. Sun and M. C. Gupta, "Laser annealing of silicon surface defects for photovoltaic applications," *Surf. Sci.* **652**, 344–349 (2016).

<sup>9</sup>Z. Hameiri, T. Puzzer, L. Mai, A. B. Sproul, and S. R. Wenham, "Laser induced defects in laser doped solar cells," *Prog. Photovolt.* **19**, 391 (2010).

<sup>10</sup>M. Abbott, P. Cousins, F. Chen, and J. Cotter, "Laser-induced defects in crystalline silicon solar cells," *Proceedings of the 31st IEEE PVSC* (IEEE, 2005), pp. 1241–1244.

<sup>11</sup>R. T. Young, R. F. Wood, and W. H. Christie, "Laser processing for high-efficiency Si solar cells," *J. Appl. Phys.* **53**, 1178–1189 (1982).

<sup>12</sup>C. Zhang, S. E. Watkins, R. M. Walser, and M. F. Becker, "Laser-induced damage to silicon CCD imaging devices," *Opt. Eng.* **30**, 651–657 (1991).

<sup>13</sup>V. K. Arora and A. L. Dawar, "Laser-induced damage studies in silicon and silicon-based photodetectors," *Appl. Opt.* **35**, 7061–7065 (1996).

<sup>14</sup>M. Ametowobla, G. Bilger, J. R. Kohler, and J. H. Werner, "Laser induced lifetime degradation in p-type crystalline silicon," *J. Appl. Phys.* **111**, 114515 (2012).

<sup>15</sup>Z. Sun and M. C. Gupta, "Laser induced defects in silicon solar cells and laser annealing," *Proceedings of the 43rd IEEE PVSC* (IEEE, 2016), pp. 713–716.

<sup>16</sup>D. L. Parker, F.-Y. Lin, S.-J. Zhu, D.-K. Zhang, and W. A. Porter, "Selective lifetime doping in silicon by laser scanning," *IEEE Trans. Electron Devices* **29**, 1718–1722 (1982).

<sup>17</sup>P. M. Mooney, R. T. Young, J. Karins, Y. H. Lee, and J. W. Corbett, "Defects in laser damaged silicon observed by DLTS," *Phys. Stat. Sol.* **48**, K31 (1978).

<sup>18</sup>Y. Matsuoka and A. Usami, "Normal laser damage of silicon solar cells without phase change," *Appl. Phys. Lett.* **25**, 574 (1974).

<sup>19</sup>J. R. Meyer, M. R. Kruer, and F. J. Bartoli, "Optical heating in semiconductors: Laser damage in Ge, Si, InSb, and GaAs," *J. Appl. Phys.* **51**, 5513–5522 (1980).

<sup>20</sup>A. Ramer, O. Osmani, and B. Rethfeld, "Laser damage in silicon: Energy absorption, relaxation, and transport," *J. Appl. Phys.* **116**, 053508 (2014).

<sup>21</sup>K. Ohmer, Y. Weng, J. R. Kohler, H. P. Strunk, and J. H. Werner, "Defect formation in silicon during laser doping," *IEEE J. Photovolt.* **1**, 183 (2011).

<sup>22</sup>A. Chantre, "Deep level defects in silicon after beam processing in the solid phase regime," *J. Phys. C* **5**, 269–280 (1983).

<sup>23</sup>Y. Weng, B. Kedjar, K. Ohmer, J. R. Kohler, J. H. Werner, and H. P. Strunk, "Dislocation formation during laser processing of silicon solar cell materials," *Phys. Status Solidi C* **10**, 28–31 (2013).

<sup>24</sup>Z. Sun and M. C. Gupta, "Laser processed silicon for photovoltaics and structural phase transformation," *Appl. Surf. Sci.* **456**, 342–350 (2018).

<sup>25</sup>K. Hou, H. Koyama, K. Uda, and Y. Miura, "Incorporation of oxygen into silicon during pulsed-laser irradiation," *Jpn. J. Appl. Phys.* **19**, L375–L378 (1980).

<sup>26</sup>S. Baumann, D. Kray, K. Mayer, A. Eyer, and G. P. Willeke, "Comparative study of laser induced damage in silicon wafers," *Proceedings of the 4th WCPEC* (IEEE, 2006), pp. 1142–1145.

<sup>27</sup>Z. Sun, M. He, L. V. Zhigilei, and M. C. Gupta, "Laser induced point defects in silicon: Combined experimental and simulation investigations" (unpublished).

<sup>28</sup>P. S. Prevey, "X-ray diffraction residual stress techniques," *Lambda Technol.* **10**, 380–392 (2006).

<sup>29</sup>P. J. Drummond, D. Bhatia, A. Kshirsagar, S. Ramani, and J. Ruzyllo, "Studies of photoconductance decay method for characterization of near-surface electrical properties of semiconductors," *Thin Solid Films* **519**, 7621–7626 (2011).

<sup>30</sup>G. Juska, K. Arlauskas, M. Viliunas, and J. Kocka, "Extraction current transients: New method of study of charge transport in microcrystalline silicon," *Phys. Rev. Lett.* **84**, 4946–4949 (2000).

<sup>31</sup>J. Wagner, "Band-gap narrowing in heavily doped silicon at 20 and 300K studied by photoluminescence," *Phys. Rev. B* **32**, 1323–1325 (1985).

- <sup>32</sup>S. E. Watkins, C. Z. Zhang, R. M. Walser, and M. F. Becker, "Electrical performance of laser damaged silicon photodiodes," *Appl. Opt.* **29**, 827–835 (1990).
- <sup>33</sup>Y. K. Jhee, M. F. Becker, and R. M. Walser, "Charge emission and precursor accumulation in the multiple-pulse damage regime of silicon," *J. Opt. Soc. Am. B* **2**, 1626–1633 (1985).
- <sup>34</sup>Y. S. Liu, S. W. Chiang, and F. Bacon, "Rapid oxidation via adsorption of oxygen in laser-induced amorphous silicon," *Appl. Phys. Lett.* **38**, 1005–1007 (1981).
- <sup>35</sup>B. J. Heijmink-Liesert, T. Gregorkiewicz, and C. A. J. Ammerlaan, "Photoluminescence of silicon thermal donors," *Phys. Rev. B* **47**, 7005–7012 (1993).
- <sup>36</sup>V. Kveder, T. Sekiguchi, and K. Sumino, "Electronic states associated with dislocations in p-type silicon studied by means of electric-dipole spin resonance and deep-level transient spectroscopy," *Phys. Rev. B* **51**, 16721–16727 (1995).
- <sup>37</sup>M. V. Shugaev, C. Wu, O. Armbruster, A. Naghilou, N. Brouwer, D. S. Ivanov, T. J. Y. Derrien, N. M. Bulgakova, W. Kautek, B. Rethfeld, and L. V. Zhigilei, "Fundamentals of ultrafast laser–material interaction," *MRS Bull.* **41**, 960–968 (2016).
- <sup>38</sup>L. Landau, "On the vibrations of the electronic plasma," *J. Phys.* **10**, 25–34 (1946).
- <sup>39</sup>J. Dawson and C. Oberman, "High-frequency conductivity and the emission and absorption coefficients of a fully ionized plasma," *Phys. Fluids* **5**, 517–524 (1962).
- <sup>40</sup>S. M. Hu, "Dislocation pinning effect of oxygen atoms in silicon," *Appl. Phys. Lett.* **31**, 53–55 (1977).
- <sup>41</sup>K. Jiptner, B. Gao, H. Harada, Y. Miyamura, M. Fukuzawa, K. Kakimoto, and T. Sekiguchi, "Thermal stress induced dislocation distribution in directional solidification of Si for PV application," *J. Cryst. Growth* **408**, 19–24 (2014).
- <sup>42</sup>I. L. Repins, W. K. Metzger, C. L. Perkins, J. V. Li, and M. A. Contreras, "Correlation between measured minority-carrier lifetime and Cu(In, Ga)Se<sub>2</sub> device performance," *IEEE Trans. Electron Devices* **57**, 2957–2963 (2010).
- <sup>43</sup>H. Huang, J. Lv, Y. Bao, R. Xuan, S. Sun, S. Sneek, S. Li, C. Modanese, H. Savin, A. Wang, and J. Zhao, "20.8% industrial PERC solar cell: ALD Al<sub>2</sub>O<sub>3</sub> rear surface passivation, efficiency loss mechanisms analysis and roadmap to 24%," *Sol. Energy Mater. Sol. Cells* **161**, 14–30 (2017).
- <sup>44</sup>M. A. Green, "Limits on the open-circuit voltage and efficiency of silicon solar cells imposed by intrinsic auger processes," *IEEE Trans. Electron Devices* **31**, 671–678 (1984).
- <sup>45</sup>J. Mattheis and J. H. Werner, "Finite mobility effects on the radiative efficiency limit of pn-junction solar cells," *Phys. Rev. B* **77**, 085203 (2008).
- <sup>46</sup>P. K. Giri, G. Galvagno, A. La Ferla, E. Rimini, S. Coffa, and V. Raineri, "Formation and annealing of defects during high-temperature processing of ion-implanted epitaxial silicon: The role of dopant implants," *Mater. Sci. Eng. B* **71**, 186–191 (2000).